Oxidation and phase transitions of epitaxial tin oxide thin films on $(\bar{1}012)$ sapphire

X. Q. Pan[a] and L. Fu
Department of Materials Science and Engineering, The University of Michigan, Ann Arbor, Michigan 48109

(Received 11 September 2000; accepted for publication 5 March 2001)

We studied the structural behavior and electrical transport properties of epitaxial α-SnO thin films grown on the $(\bar{1}012)$ α-Al_2O_3 (sapphire) substrate. Hall effect measurements revealed that the epitaxial as-deposited SnO film is a *p*-type semiconductor. *In situ* x-ray diffraction studies show that the α-SnO phase is metastable and will transform into SnO_2 with the rutile type structure when annealed at high temperatures in air. The onset of this phase transformation was observed to begin approximately at 300 °C during heating. Shortly thereafter, rutile SnO_2 was observed to coexist with α-SnO and intermediate products such as Sn and Sn_3O_4. After being annealed at temperatures above 600 °C, the film then fully transformed into the rutile SnO_2 phase. Our results show that the α-SnO to SnO_2 structural transformation proceeds initially by the localized disproportionate redistribution of internal oxygen at low temperature, followed by the transformation of the remaining SnO phase and intermediate phases into SnO_2 via the inward diffusion of external oxygen at higher temperatures. Most of the SnO_2 crystallites nucleate epitaxially on α-SnO with the orientation relationship of $(101)_{SnO_2}//(001)_{SnO}$ and their growth processes are controlled by the $(101)_{SnO_2}//(001)_{SnO}$ interfaces, leading to a (101) texture and a laminar grain shape for SnO_2. The relationship between the electrical transport properties and the structural evolution of the film has also been investigated. [DOI: 10.1063/1.1368865]

I. INTRODUCTION

Tin dioxide (SnO_2) with the rutile type structure is an *n*-type wide band-gap semiconductor. Due to its outstanding electrical, optical, and electrochemical properties, SnO_2 has a wide range of applications in solar cells, catalytic support materials, transparent electrodes, and solid state chemical sensors.[1,2] SnO_2 is widely used as a base material in gas alarms on domestic, commercial, and industrial premises due to its high sensitivity to small concentrations of gases (at ppm levels). In particular, SnO_2 thin films have drawn much interest because of their potential application in transparent electrodes for solid state display and microelectronic gas sensing devices.[3] Considerable attention has recently focused on the development of solid state gas sensors based on nanocrystalline thin films.[4–10]

Physical vapor deposition (PVD) methods have been widely used for the fabrication of tin oxide thin films.[11–15] SnO_2 ceramics are commonly used as source material. Under high vacuum conditions and at high temperatures, the gaseous SnO_2 molecules will dissociate and the film material condensed onto the substrate is primarily oxygen deficient. Previous studies[16,17] have shown that films deposited at low substrate temperatures (below 300 °C) are amorphous, while films grown above 350 °C have a crystalline α-SnO structure. Such oxygen-deficient phases are metastable in air. A postdeposition annealing in oxygen atmosphere is required in order to obtain a rutile SnO_2 film.

The postdeposition annealing process has a strong influence on the microstructure, chemical composition, and electrical transport properties of the resulting SnO_2 films. Geurts *et al.*[18] used Raman scattering, IR reflectivity measurements, and x-ray diffraction (XRD) to examine the oxidation process that converts electron beam evaporated SnO films into SnO_2. They concluded that the oxidation process began with the formation of SnO_2 and other intermediate phases, such as Sn_3O_4 and metallic Sn, via internal oxygen disproportionate allocation, which was then followed by external oxygen in-diffusion to complete the transformation. Reddy *et al.*[16] reported that electron-beam evaporated tin oxide films transform into the final oxidation state SnO_2 either through the single oxidation state SnO or through two oxidation states, namely SnO and Sn_3O_4, depending on the film deposition temperature. Soares *et al.*[19] studied tin oxide films prepared by reactive sputtering using Mössbauer spectroscopy. They found that films grown with low oxygen pressure retained a certain amount of SnO even after annealing at 600 °C, while those deposited at high oxygen pressure were completely transformed to SnO_2 even though they were annealed at the same temperature.

Although many studies have been reported on the annealing process of SnO_x films, the α-SnO–SnO_2 phase transformation mechanisms are still unclear. In particular, little work has been done on the influence of the oxidation processes on the microstructure, crystal defect configurations, and electrical transport properties of the resulting SnO_2 thin films. This knowledge is crucial to establish the structure–property relationships of SnO_2 thin films. In the present study, epitaxial SnO thin films were deposited on sapphire

[a]Electronic mail: panx@umich.edu

substrates and their structural evolution during annealing at high temperatures in air were investigated by *in situ* x-ray diffraction, transmission electron microscopy (TEM), x-ray photoelectron spectroscopy, and Hall effect measurements using the van der Pauw method. The structure–property relationships of the SnO during the transformation processes has been established based on the experimental observations.

II. EXPERIMENTAL METHODS

SnO thin films were deposited on $(\bar{1}012)$ α-Al_2O_3 (sapphire) substrates by the electron beam evaporation of SnO_2 ceramic source. The disks of SnO_2 ceramic were prepared by sintering a high purity SnO_2 powder synthesized by chemical coprecipitation. A detailed description of the experimental procedure is given elsewhere.[17] The substrate materials used in this study were single-crystal α-Al_2O_3 with a $(\bar{1}012)$ surface orientation (R-cut). After loading the substrate into the deposition chamber, the system was pumped down to approximately 5.0×10^{-8} Torr. During deposition, the background pressure in the chamber was about 10^{-6} Torr. Films were deposited at 600 °C with a nominal film thickness around 1000 Å. A quartz crystal oscillator installed within the deposition chamber was used to measure the deposition rate and film thickness during deposition. The film thickness measurement was ascertained by cross-section TEM. The deposition rate for this study was 0.4 Å/s.

In situ x-ray diffraction (XRD) studies were carried out on a Rigaku diffractometer using Cu $K\alpha$ radiation. Samples were oxidized at high temperature in air. Some of the XRD studies at room temperature were conducted on a rotating anode four-circle diffractometer (Rigaku, Japan). TEM examinations were conducted in a JEOL 4000EX high-resolution transmission electron microscope (HRTEM) equipped with a Gatan imaging filter (GIF). The microscope was operated at 400 kV, which provides a point-to-point resolution of 0.17 nm. Cross-sectional TEM specimens were prepared by a standard procedure, which includes mechanical grinding, polishing, precision dimpling, and ion milling. The final thinning of specimens was carried out on a Gatan precision ion polishing system (PIPS™, Model 691) using an accelerating voltage of 4.5 kV and an incident angle of 4°–6°. X-ray photoelectron spectroscopic (XPS) studies were performed on a PHI 5400 XPS system (Perkin-Elmer Corporation, MN). All spectra were recorded under vacuum condition better than 10^{-9} Torr. The electrical properties of the thin films were determined by Hall effect measurements in a 2.5×10^3 Gauss magnetic field using the van der Pauw method.

III. RESULTS

As reported in previous work,[17] an epitaxial α-SnO thin film can be fabricated on a $(\bar{1}012)$ sapphire (α-Al_2O_3) substrate by electron beam evaporation deposition at 600 °C using a ceramic SnO_2 source. As-deposited epitaxial α-SnO film was loaded into a hot-stage for *in situ* XRD study. X-ray diffraction patterns were recorded at various temperatures between room temperature and 700 °C during heating in air.

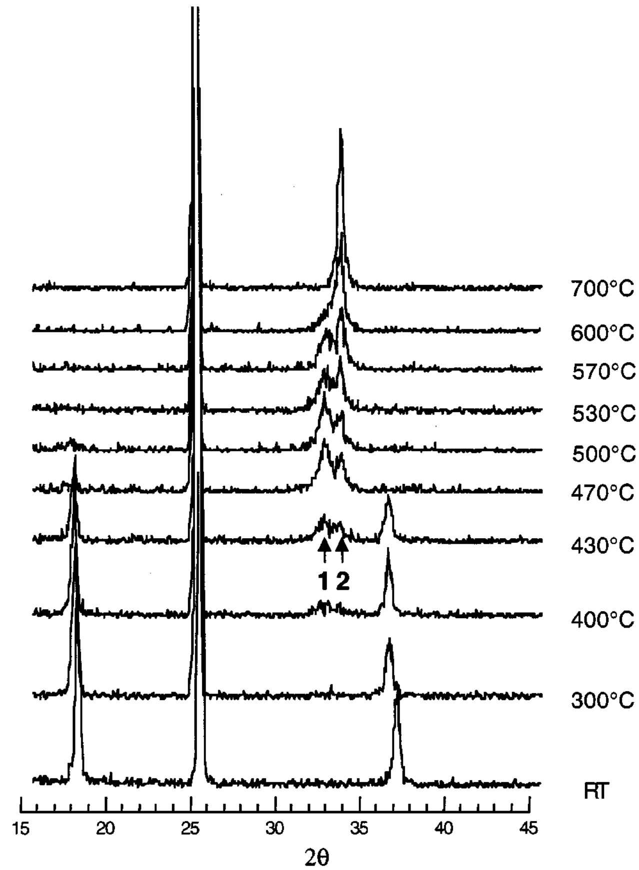

FIG. 1. *In situ* XRD spectra showing the phase transformation from SnO to SnO_2. The strong reflection peak around 25° is from substrate. Peak 1 is from Sn_3O_4 (003) and peak 2 is from SnO_2 (101).

Figure 1 shows XRD patterns of the film recorded at different temperatures upon heating. All diffraction patterns were recorded in a 2θ range of 15°–85°. However, only data from 15° to 45° is shown in Fig. 1 since no useful information exists from 45° to 85°. The first diffraction pattern was taken at room temperature before heating. The film was slowly heated to 300 °C and held at this temperature for 1 h before the next diffraction pattern was recorded. Subsequently, the temperature was increased stepwise at a rate of 2 °C/min. The sample was kept at each hold temperature step for 30 min before recording an XRD pattern, which itself took about 35 min. After the final diffraction spectrum was captured at 700 °C the film was cooled down to room temperature at a rate of 5 °C/min.

As seen in Fig. 1, the only difference between the XRD pattern recorded at room temperature and that recorded at 300 °C is the shift of the SnO *001* ($2\theta=18.3°$) and *002* ($2\theta=37.2°$) peaks towards a small 2θ value which is caused simply by the thermal expansion of the lattice constant on heating. This result indicates that there is no visible phase change occurring in the film up to 300 °C. Starting from 400 °C, the intensity of the SnO *001* and *002* reflections decreases and new peaks appear in the spectrum, which indicates that a phase transformation has occurred in the system. The broad peak at 31°–34° is a superposition of two reflections (peak 1 at 32.2° and peak 2 at 33.1°). Comparing this XRD pattern with standard powder diffraction patterns for

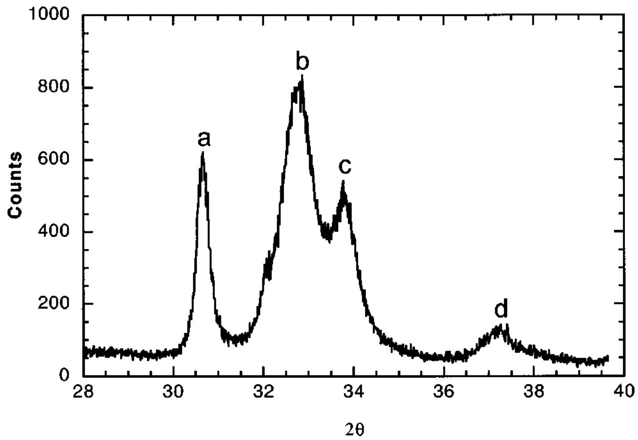

FIG. 2. High resolution XRD pattern taken from the film annealed at 500 °C for 5 min, showing the appearance of several phases including SnO, Sn_3O_4, and SnO_2. (a) β-Sn *100* reflection, (b) Sn_3O_4 *003* reflection, (c) SnO_2 *101* reflection, and (d) SnO *002* reflection.

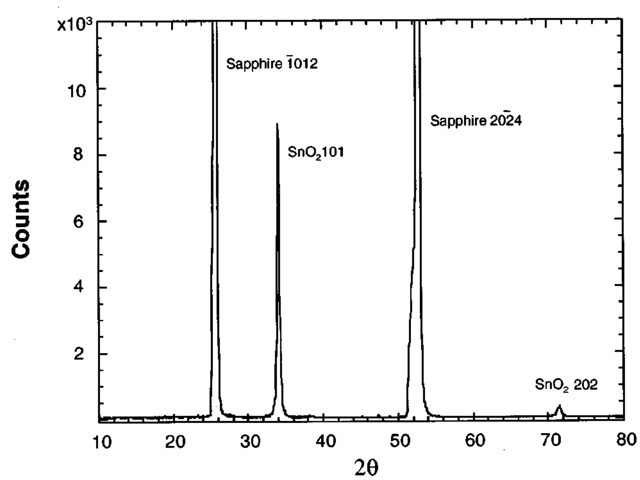

FIG. 3. θ–2θ scan taken at room temperature from the same sample as for Fig. 1 after finishing *in situ* XRD studies. Note that SnO_2 is the only phase in the film and that an out-of-plane texture exists.

α-SnO, SnO_2, and other possible tin oxide phases, peak 2 represents the SnO_2 (101) plane (2θ of 33.9° at room temperature), while peak 1 may correspond to the *003* reflection of a metastable Sn_3O_4 phase (2θ of 32.9° at room temperature). Upon further heating, the SnO *001* and *002* peaks become shorter and broader and disappear at 500 °C, while the intensities of peak 1 and peak 2 increase gradually. When the temperature is increased further, peak 1 starts to diminish and disappears at ~600 °C, whereas peak 2 continues to grow and becomes the only reflection from the film in the diffraction pattern, indicating the completion of the phase transformation from the α-SnO to the rutile SnO_2 phase.

From these *in situ* XRD studies we see that Sn_3O_4 is an intermediate phase in the temperature range between 400 and 500 °C during the phase transformation from SnO to SnO_2. When the temperature increases above 500 °C, the Sn_3O_4 phase is transformed into the rutile SnO_2 phase. The XRD patterns in Fig. 1 show that most of the Sn_3O_4 phase has transformed into SnO_2 at 600 °C. Rutile SnO_2 is the only phase visible in XRD patterns from the film annealed at 700 °C. The final SnO_2 film has an out-of-plane orientation relationship with respect to the substrate of $SnO_2(101)\|Al_2O_3(\bar{1}012)$.

It was reported in the literature that internal oxygen disproportionate distribution at intermediate temperatures (~400–500 °C) leads to metallic tin segregation during the heating and annealing processes.[18] However, no reflection peaks corresponding to metallic tin were found in our *in situ* XRD study. Since the intensity of the x-ray diffractometer used for our *in situ* investigations was quite low, it was possible that the weak metallic tin reflection peaks could not be detected in that particular XRD apparatus. In order to elucidate the situation, a sample, which was cut from the same as-deposited film for the *in situ* XRD studies, was annealed at 500 °C for 5 min in a tube furnace at a heating and cooling rate of 10 °C/min. A high resolution θ–2θ XRD pattern of this film was then recorded using a rotating anode four circle x-ray diffractometer, as shown in Fig. 2. Peaks *b* and *c* correspond to the Sn_3O_4 *003* reflection and SnO_2 *101* reflection, respectively. Peak *a*, located at 30.7° in 2θ, is identified to be the *100* reflection of β-Sn, which has a tetragonal structure. Peak *d* is the reflection from the SnO *002* plane. These results clearly show that metallic Sn precipitates indeed exist in the film at the intermediate stage of the SnO to SnO_2 transformation process and that annealing at 500 °C for 5 min does not complete the transformation. Figure 3 is a high-resolution x-ray diffraction scan taken from the sample which was cooled down from 700 °C upon completion of the *in situ* XRD study, as previously described (see Fig. 1). Except for the strong peaks from the substrate, the only other visible reflections belong to SnO_2 *101* and *202*, indicating that the SnO to SnO_2 transformation is complete and that the film has a strong (101) texture.

Figure 4(a) is a plane-view TEM image taken from the specimen that was examined by *in situ* XRD used for Figs. 1 and 3. The average grain size in the film is about 100 nm. The corresponding electron diffraction pattern is shown in Fig. 4(b), which was recorded with the electron beam aligned perpendicular to the sapphire substrate surface $(\bar{1}012)$. The diffraction pattern shows some high intensity spots located on the ring pattern of the rutile SnO_2 structure. This indicates the existence of an in-plane texture in the SnO_2 film. Figure 4(c) is a cross-section TEM micrograph taken from the same film. A laminar grain morphology is seen in the film. The average thickness of the laminas is about 20 nm, which is much smaller than the lateral dimension (~100 nm) as revealed by the plan-view and cross-section images in Figs. 4(a) and 4(c).

Many crystal defects, including twin boundaries and crystallographic shear planes (CSP), are found in the SnO_2 film transformed from α-SnO. Figure 5 is an HRTEM micrograph of the same specimen as shown in Fig. 4, showing the existence of defects. Twin boundaries and CSPs, indicated by arrows in the image, are normally located parallel to the SnO_2 (101) plane, which is parallel to the film surface. Some of these defects terminate within crystallites. Many of the SnO_2 crystallites are multiply twinned. The existence of multiply twinned nanocrystallites may result from deforma-

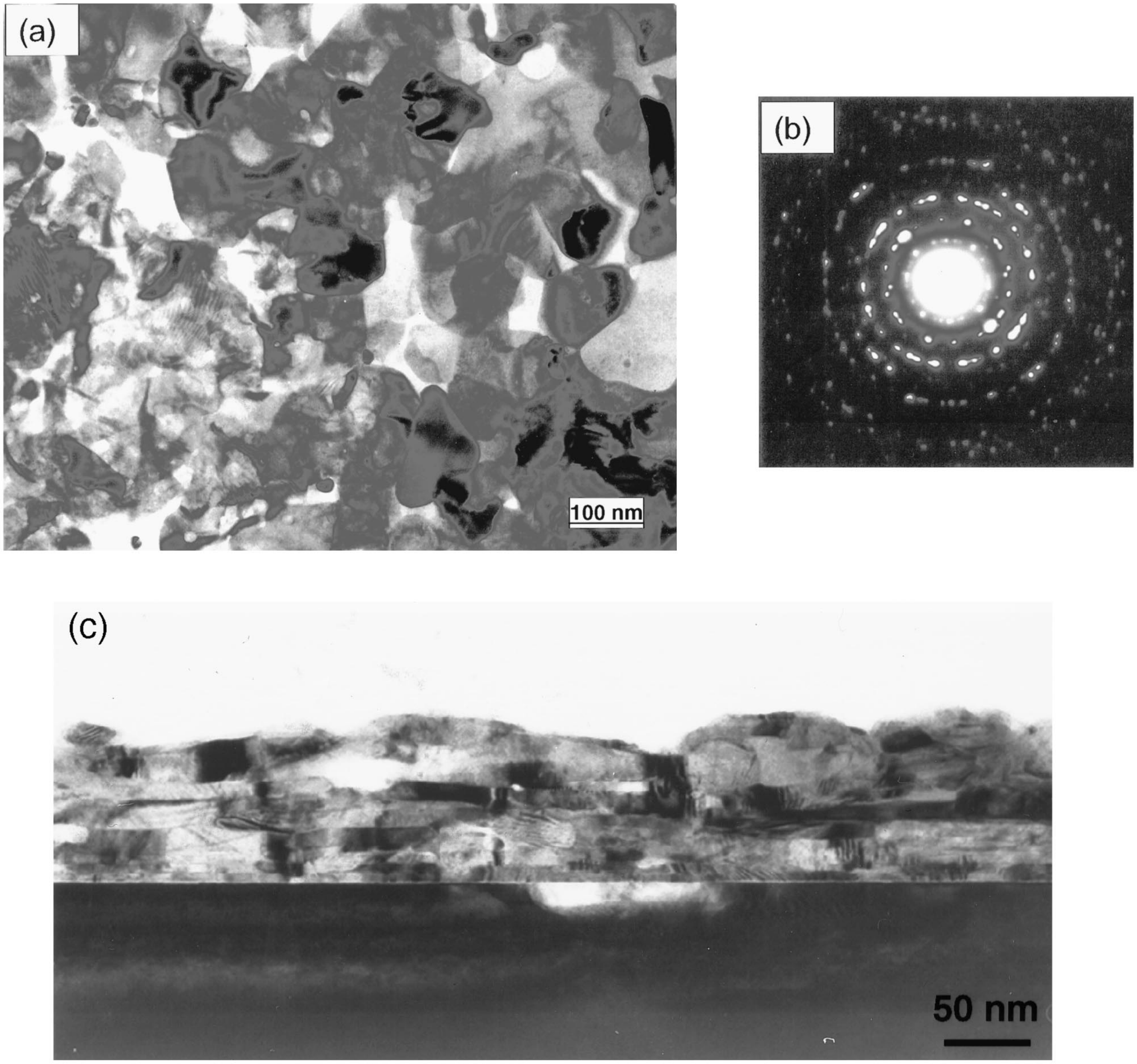

FIG. 4. (a) Plane-view TEM micrograph of the film annealed at 700 °C, (b) corresponding selected area electron diffraction, and (c) cross-section micrograph of the same film. Note the layered microstructure of SnO_2 films.

tion stresses applied on the SnO_2 crystallites during the phase transformation from SnO to SnO_2.

The microstructure evolution during the phase transformation of the film was also studied using TEM. Figure 6(a) shows a cross-sectional TEM image taken from the film annealed at 500 °C for 5 min (the sample examined for Fig. 2). We see that the film consists of regions with different microstructures. This feature is clearly shown in Fig. 6(b), which is an enlarged image from the region marked by a rectangle in Fig. 6(a). The area marked by the letter R is identified to be the rutile-type SnO_2 phase which results in the strong Bragg spots in the electron diffraction pattern of the film, shown as an inset in the upper right corner of Fig. 6(b). The diffraction pattern also has diffused streaks and satellite spots along the film normal which are caused by regions in the film consisting of long, parallel lamellas as seen in Fig. 6(a). An example is shown in the middle region of Fig. 6(b), where there exist a number of closely spaced stacking faults. Some metastable phases with periodically spaced CSPs in the rutile lattice structure were observed due to oxygen deficiency in the film, which lead to the occurrence of satellite reflections in the electron diffraction pattern. Such metastable phases are similar to the defect structures found in nonstoichiometric TiO_{2-x}.[20]

Chemical compositions of the films were studied by XPS. Figure 7 shows XPS spectra for core levels Sn $3d_{5/2}$, Sn $3d_{3/2}$, and O 1s of three films at different oxidation stages. The lower spectra in Figs. 7(a) and 7(b) were recorded from the epitaxial α-SnO film before annealing, while the upper spectra were taken from the film which was studied by *in situ* XRD, as described previously. As shown before, XRD and TEM studies indicated that the latter sample consists of only a rutile SnO_2 structure (see Figs. 1 and 3–5). The spectra in the middle were collected from the film that

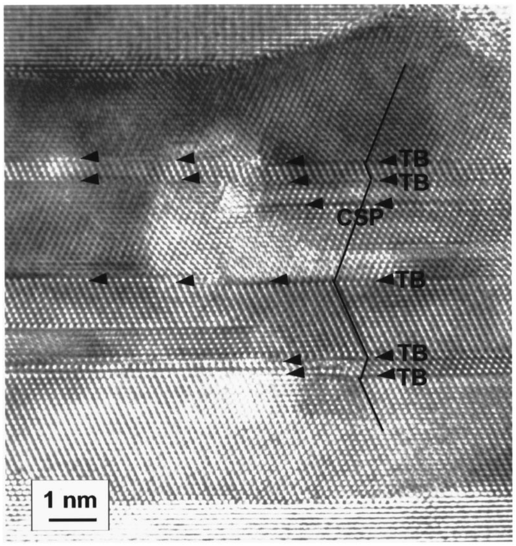

FIG. 5. HRTEM image of a SnO_2 film showing the existence of crystal defects (twin boundary and crystallographic shear plane).

was annealed at 500 °C for 5 min. The corresponding XRD and TEM results are shown in Figs. 2 and 6. Comparing these XPS spectra, we see that the Sn $3d_{5/2}$ and $3d_{3/2}$ peaks are shifted toward high binding energy during the SnO–SnO_2 phase transformation, which corresponds to an increase of the work function (higher oxidation states) due to the difference in the coordination and bonding characteristics

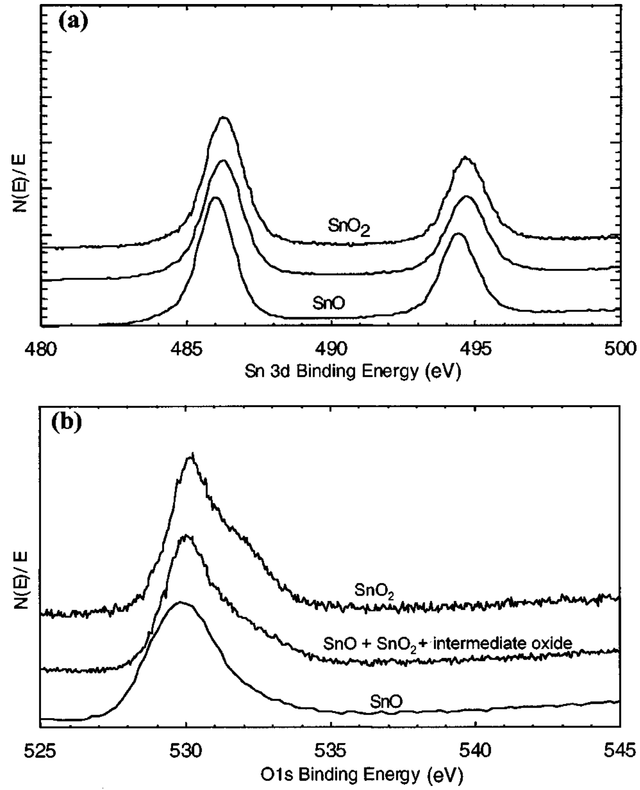

FIG. 7. XPS spectra showing the binding energy of Sn 3d (a) and O 1s (b).

of Sn in SnO and SnO_2 phases. It has been reported that the O 1s peak in oxides resides in the energy region of 529–532 eV.[21] The peak around 529 to 530 eV is commonly ascribed to lattice oxygen. Ghuang *et al.*[22] found that the peak around 530.7–531.6 eV is caused by oxygen inside nonstoichiometric oxides within the surface region of the material. Srinivasan *et al.*[23] ascribed the peak at 531.7 eV to be chemisorbed oxygen on the surface. According to these studies, the

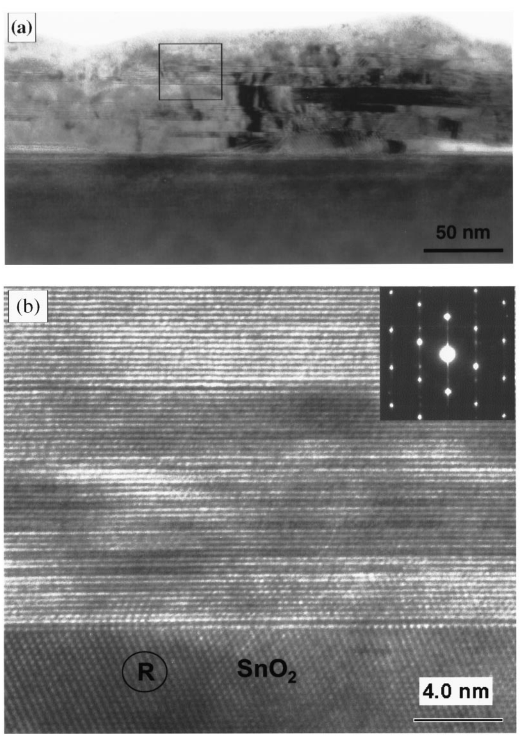

FIG. 6. (a) Cross-section TEM micrograph taken from the film annealed at 500 °C for 5 min. (b) Enlarged image from the area marked by a square in (a). The layer indicated by R is identified to be the rutile type SnO_2. The inset in the upper right-hand side of (b) shows the corresponding electron diffraction pattern.

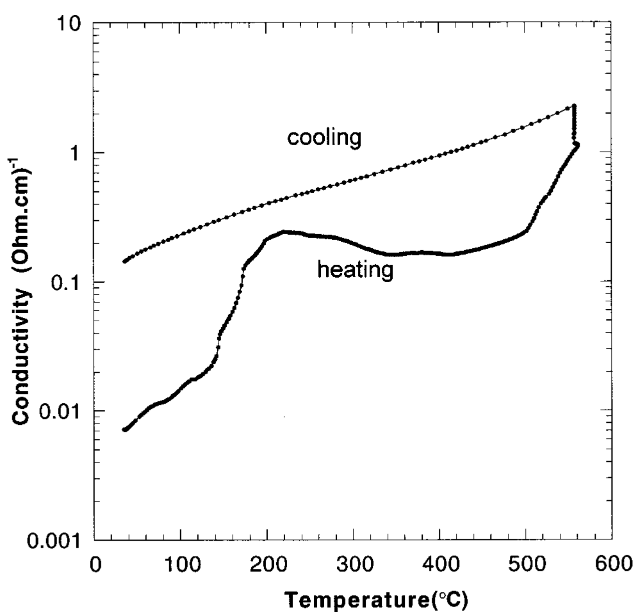

FIG. 8. Electrical conductivity of tin oxide film as a function of temperature on heating and cooling.

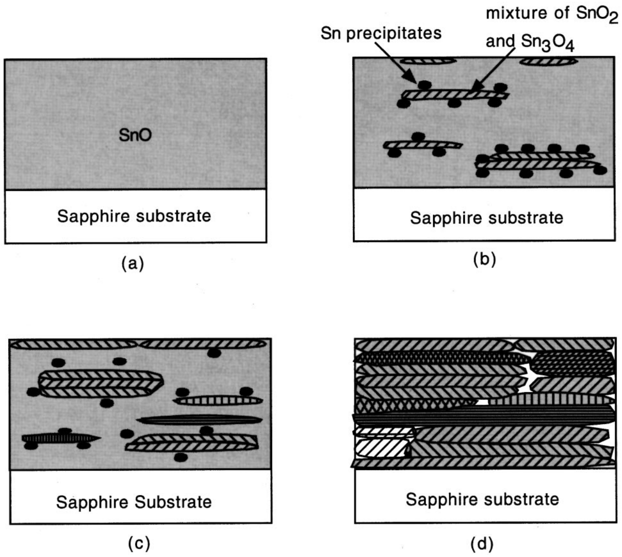

FIG. 9. Schematics showing the SnO–SnO_2 structural transformation during heating in air. (a) as-deposited film, (b) oxygen disproportionation inside the film, (c) growth of the laminas and oxygen diffusion, and (d) final SnO_2 film.

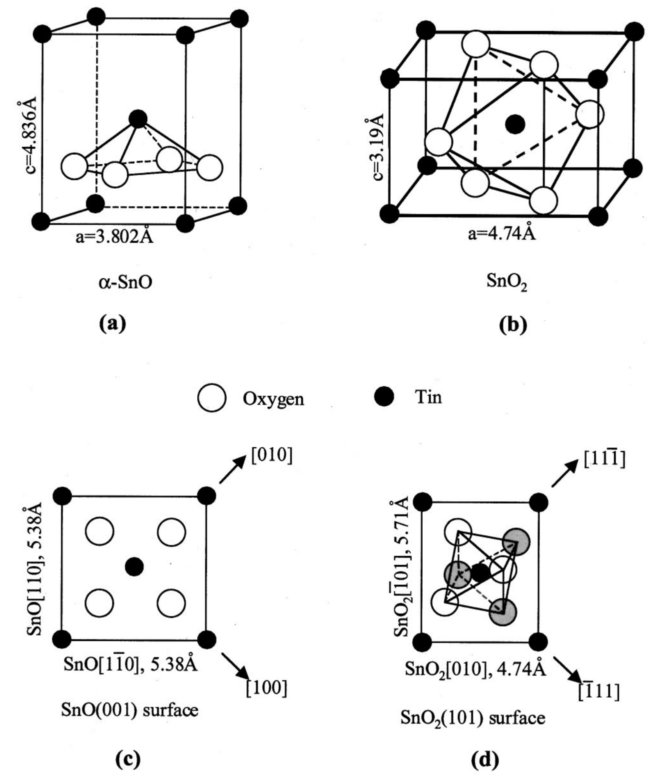

FIG. 10. (a) Unit cell of SnO, (b) unit cell of SnO_2, (c) atomic configurations of the SnO (001) surface, and (d) atomic configurations of the SnO_2 (101) surface.

peaks at 530 eV in Fig. 7(b) can be attributed to lattice oxygen in the tin oxide films. The nonsymmetric part of the O 1*s* peak around 532 eV may be due to chemisorbed oxygen on the surface of SnO_2 crystallites in the annealed film. The relative concentrations of the constituent elements in the films were calculated by utilizing peak area sensitivity factors. The [Sn]/[O] ratio was found to be 49.2/50.8, 42.4/57.6, and 32.3/67.7 for the as-grown film, the film annealed at 500 °C and the film annealed at 700 °C, respectively.

Electrical transport properties of the tin oxide film were performed by both electrical conductivity measurements and Hall effect measurements at different temperatures during annealing in synthesized air. The measurements were conducted using a four-point probe (van der Pauw) method. The as-grown epitaxial SnO film was heated from ambient temperature (~22 °C) to 560 °C at a rate of 2°/min and held at this temperature for 10 h. The cooling run was also conducted at a rate of −2°/min. The conductivity as a function of temperature was recorded during heating and cooling, as shown in Fig. 8. Up to 200 °C during heating, film conductivity increased with the increase of temperature. However, the slope of the conductivity–temperature ($\sigma - T$) curve changed at ~140 °C. Above 140 °C, the conductivity rapidly increased with increasing temperature. When heated to about 200 °C, the slope of the curve changed again and the conductivity slightly decreased with the further increase of temperature up to ~400 °C. Subsequently, the conductivity increased with increasing temperature. On cooling, after annealing at 560 °C for 10 h, the film showed a conductivity–temperature relationship of $\sigma = \sigma_0 \exp(E/kT)$, which is a typical feature for a rutile type SnO_2 film. After the film was cooled down to room temperature, the XRD (θ–2θ) pattern was recorded. The diffraction pattern (not shown here) is similar to that shown in Fig. 3, indicating that the film consists of the rutile SnO_2 phase. The Hall measurements were also conducted on the same as-deposited film from ambient temperature to 375 °C. It was found that the film shows the typical transport behavior of a *p*-type semiconductor up to 350 °C and the combined effects of both *p*- and *n*-type semiconductors above such temperature.

IV. DISCUSSION

The experimental results described above show that epitaxial α-SnO film grown on $(\bar{1}012)$ α-Al_2O_3 substrate is unstable in oxygen atmosphere at high temperature and will transform into the rutile SnO_2 phase through an oxidation process. If the phase transformation in the epitaxial SnO film proceeds only through the diffusion of oxygen from annealing atmosphere, the phases with high oxidation states (Sn_3O_4 and SnO_2) should mainly be located near the film surface at the initial stage and the metallic tin phase should not form in the film. However, the XRD results of the partially oxidized film clearly demonstrate the coexistence of the rutile SnO_2 phase with many other intermediate products, such as Sn_3O_4 and metallic tin. Cross-section TEM studies of the film quenched from the intermediate annealing stage also show that rutile SnO_2 and other intermediate oxidation products are distributed randomly in the film. This means that the oxidation of the SnO film proceeds both through the surface reaction with atmospheric oxygen and through internal oxidation by local disproportionate oxygen distribution. The latter process is particularly important at relatively low temperature at which oxygen diffusion in the crystal lattice is slow. As proposed by Geurts *et al.*,[18] this process can be considered as

$$(1+x)\mathrm{SnO} \rightarrow x\mathrm{Sn}+\mathrm{SnO}_{1+x}.$$

This reaction leads to the coexistence of SnO with higher oxidation states (Sn_3O_4 and SnO_2) and precipitation of the metallic tin phase. Further oxidation requires additional oxygen to transform SnO_x and metallic Sn into the rutile SnO_2. This process becomes more efficient when the temperature is increased, due to enhanced oxygen diffusion at high temperatures. The mechanisms of the SnO–SnO_2 structural transformation discussed are schematically shown in Figs. 9(a)–9(d).

Both XRD and TEM studies show that the SnO_2 film obtained by annealing at high temperature consists of a (101) texture. To understand the formation mechanism of the (101) texture in SnO_2 film, it is necessary to study the atomic structures of both α-SnO and SnO_2. Both of these materials are tetragonal, and the unit cells of both structures are shown in Figs. 10(a) and 10(b). In the rutile SnO_2 structure each Sn atom has six nearest oxygen neighbors, which form a distorted octahedron. Sn atoms fill the center of the oxygen octahedra. The distance between Sn and O atoms within one octahedron is 2.057 Å. On the other hand, α-SnO has a layered atomic structure, similar to that of PbO. Each Sn atom has four nearest oxygen neighbors, but all of these oxygen atoms are located on the same side of the Sn atom, as shown by the pyramid consisting of one Sn atom and four O atoms in the SnO unit cell [Fig. 10(a)]. The Sn–O bond has a length of 2.223 Å.

There is a marked similarity between the (001) surface of SnO and the (101) surface of SnO_2, as shown in Figs. 10(c) and (d). In Fig. 10(c), oxygen atoms are located at the same level above the Sn atomic layer. Oxygen atoms, shown as open circles and shaded circles in Fig. 10(d) are located, respectively, below and above the Sn (closed small circles) atomic layer. It can be seen that when a (101) epilayer of the rutile SnO_2 phase forms on the SnO (001) surface, only a small distortion of Sn sublattice is required. However, the oxygen configurations on SnO (001) and SnO_2 (101) surfaces are quite different. Due to the onefold symmetry on the (101) SnO_2 surface and fourfold symmetry on the (001) SnO surface, four different rotational variants of SnO_2 phase may occur in the film: $[010](101)_{SnO_2} \| [1\bar{1}0](001)_{SnO}$ and its three variants by rotation around the SnO [001] axis by $\pm 90°$ and 180°. The growth of the new SnO_2 phase proceeds through oxygen diffusion through the crystal lattice and requires the reconstruction of the oxygen sublattice for the SnO phase. It is known that the (101) surface of SnO_2 has a low surface energy. It is also seen in Fig. 10(a) that α-SnO has a (001) layered structure in the oxygen sublattice. These factors indicate that the structural transformation is controlled by the SnO–SnO_2 interface. This in turn leads to the formation of a flat SnO–SnO_2 interface and the development of the low surface energy (101) texture in SnO_2.

The formation of SnO_2 (101) orientated laminas in the films can be explained based on the oxidation mechanisms and the interface-controlled growth mechanism of the SnO_2 phase. During the initial stages of oxidation, a combination of the disproportionate redistribution of internal oxygen and the diffusion of external oxygen permits multiple phases (Sn, SnO, Sn_3O_4, and SnO_2) to coexist in the film. As discussed previously, the growth of the localized SnO_2 phase within the film is controlled by the $(101)_{SnO_2} \| (001)_{SnO}$ interface. Therefore a laminar shape of the SnO_2 crystallites is expected. This prediction is consistent with direct cross-section TEM observations, as shown in Fig. 6. As the temperature is increased, external oxygen can diffuse into the film. The SnO_2 crystallites will grow at the expense of intermediate product phases such as Sn_3O_4 and metallic tin, but the laminar shape of SnO_2 grains will remain because of the low surface energy of the (101) surface. For SnO_2 grains formed directly on the original α-SnO phase, four different in-plane orientation relationships with respect to SnO may exist, as discussed previously. These orientation relationships explain the diffraction spots with high intensities in Fig. 4(b). However, the SnO_2 grains transformed from the intermediate phases, such as Sn and Sn_3O_4 phases, may not have in-plane texture. As a result, the electron diffraction of the annealed film also consists of a ring pattern, as shown in Fig. 4(b).

Conductivity change during heating is related to both structure and composition changes in the film. The corresponding Hall measurements show that α-SnO is a *p*-type semiconductor. Electrical conduction in the material comes from the excess of oxygen, as described in previous studies.[17] On the other hand, SnO_2 is an *n*-type semiconductor and the electrical carriers (electrons) are caused by the existence of oxygen vacancies in the material. Since oxygen concentration plays an important role in the conduction mechanism of both materials, it is obvious that the anneal processes in oxygen atmosphere will have an effect on the conductivity of the film. According to the *in situ* XRD studies, SnO is the major phase at low temperature up to about 300 °C. The increase of film conductivity below 140 °C is due to the thermal activation of the *p*-type semiconductor SnO. The change in the slope of the $\sigma - T$ curve at 140 °C may be caused by the activation of chemical reactions between adsorbed oxygen atoms and SnO surfaces. This reaction can cause the increase of oxygen concentration and thus create a number of holes near SnO surfaces, which leads to the increase of electrical conductivity.

Above 200 °C, although the oxygen diffusion in the crystal lattice is limited, SnO_2 phases can form at the film surface due to reactions with chemisorbed oxygen on the surface. This was confirmed by the cross-section TEM studies of a SnO film annealed in air at 200 °C for 2 h, showing a number of small SnO_2 crystallites at the film surface. With a further increase in temperature, an internal oxidation process occurs due to the localized disproportionate redistribution of oxygen in SnO film, as revealed by *in situ* XRD studies. This internal oxidation process leads to the formation of metallic tin, Sn_3O_4, and SnO_2. The SnO_2 crystallites formed during such internal oxidation processes are usually deficient in oxygen due to a low oxygen concentration of the film ([Sn]/[O] ratio close to one). Thus they are an *n*-type semiconductor. On the other hand, the existence of small metallic tin precipitates and laminar SnO_2 crystallites in a *p*-type α-SnO matrix will form a number of phase boundaries (interfaces) in the film. A number of *p*-*n* junctions (depleted of electrical carriers) will form at the interfaces between the SnO_2 crystallites and the SnO matrix. Similarly, Schottky barriers will be formed between the *n*-type semiconductive SnO_2 crystallites and metallic Sn precipitates. As a consequence of the formation of *p*-*n* junctions and Schottky barriers, both the concentration and the mobility of electrical carriers in the film will be reduced. These processes subsequently lead to the decrease of conductivity with the increase of temperature. With a further increase in the temperature, the oxidation process becomes fast due to external oxygen diffusion from the film surface. The SnO_2 crystallites grow rapidly at the expense of other phases with low oxidation states and thereby become the major phase in the film. Due to the vanishing of the SnO phase and tin precipitates, the effect of *p*-*n* junctions and Schottky barriers on electrical transport behavior becomes small. Therefore the conductivity of the film is expected to increase with increasing temperature (see the $\sigma-T$ curve above 500 °C in Fig. 8). After annealing at 560 °C for 10 h, the film shows typical *n*-type semiconductor behavior on cooling (see Fig. 8).

V. CONCLUSIONS

Structural evolution and electrical conduction characteristics of epitaxial α-SnO thin films grown on $(\bar{1}012)$ sapphire (α-Al_2O_3) substrate have been studied in detail by different characterization methods. *In situ* x-ray diffraction studies showed that this metastable phase transforms into SnO_2 with the rutile type structure when heated to high temperatures in oxygen atmosphere. The transformation begins at about 300 °C on heating. In the initial stage of the oxidation processes, the rutile SnO_2 phase coexists with the α-SnO phase and intermediate products such as Sn and Sn_3O_4. After being annealed at temperatures above 600 °C, the film is fully transformed into the rutile SnO_2 phase. The transformation proceeds through the local disproportionate redistribution of internal oxygen at low temperature, followed by the transformation of the remaining SnO phase and the intermediate phases into SnO_2 through the inward diffusion of external oxygen at higher temperatures. The formation and growth of SnO_2 crystallites in the α-SnO film are controlled by the $(101)_{SnO_2}\|(001)_{SnO}$ interfaces, leading to a (101) texture and a laminar grain shape of SnO_2. The electrical conduction characteristics were related with events pertinent to the structural evolution of the film.

ACKNOWLEDGMENTS

The authors gratefully acknowledge the financial support of the National Science Foundation DMR 9875405 (CAREER-XQP), the Petroleum Research Fund No. 34093-G5, the College of Engineering at the University of Michigan, and the Applied Materials Company (Santa Clara, CA).

[1] *Sensors—A Comprehensive Survey*, edited by W. Göpel, J. Hesse, and J. N. Zemel (VCH Weinheim, New York, 1991), Vol. 2.
[2] K. Ihokura and J. Watson, *The Stannic Oxide Gas Sensor—Principles and Applications* (CRC, Boca Raton, FL, 1994).
[3] G. Advani and A. Jordan, J. Electrochem. Soc. **123**, 29 (1990).
[4] N. Yamazoe, Proceedings of the Third International Meeting Chem. Sensors, Cleveland, OH, 1990, pp. 3–8.
[5] C. Xu, J. Tamaki, M. Miur, and N. Yamazoe, Sens. Actuators B **3**, 147 (1991).
[6] W. Göpel and K. D. Schierbaum, Sens. Actuators B **26–27**, 1 (1995).
[7] J.-G. Zheng, X. Q. Pan, M. Schweizer, U. Weimar, W. Göpel, and M. Rühle, Philos. Mag. Lett. **73**, 93 (1996).
[8] J.-G. Zheng, X. Q. Pan, M. Schweizer, F. Zhou, U. Weimar, W. Göpel, and M. Rühle, J. Appl. Phys. **79**, 7688 (1996).
[9] J.-G. Zheng, X. Q. Pan, M. Schweizer, U. Weimar, W. Göpel, and M. Rühle, J. Mater. Sci. **31**, 2317 (1996).
[10] X. Q. Pan and J. G. Zheng, Mater. Res. Soc. Symp. Proc. **472**, 87 (1997).
[11] N. Y. Shishkin, I. M. Zharsky, V. G. Lugin, and V. G. Zarapin, Sens. Actuators B **48**, 403 (1998).
[12] M. C. Horrillo, P. Serrini, J. Santos, and L. Manes, Sens. Actuators B **45**, 193 (1997).
[13] S. Semancik and R. E. Cavicchi, Thin Solid Films **206**, 81 (1991).
[14] M. H. Reddy and A. N. Chandorkar, Sens. Actuators B **9**, 1 (1992).
[15] W. I. Cho, H. Jang, and S. R. Lee, Scr. Metall. Mater. **32**, 815 (1995).
[16] M. H. Reddy, S. R. Jawalekar, and A. N. Chandorkar, Thin Solid Films **169**, 117 (1989).
[17] L. Fu and X. Q. Pan, J. Electroceram. (submitted).
[18] J. Geurts, S. Rau, W. Richter, and F. J. Schmitte, Thin Solid Films **121**, 217 (1984).
[19] M. R. Soares, P. H. Dionisio, I. J. R. Baumvol, and W. H. Schreiner, Thin Solid Films **214**, 6 (1992).
[20] L. A. Bursill and B. G. Hyde, Acta Crystallogr., Sect. B: Struct. Crystallogr. Cryst. Chem. **B27**, 210 (1971).
[21] C. D. Wagner, W. M. Riggs, L. E. Davis, and J. F. Moulder, *Handbook of X-ray Photoelectron Spectroscopy* (Perkin-Elmer Corporation, Minnesota).
[22] T. J. Chuang, C. R. Brundle, and D. W. Rice, Surf. Sci. **59**, 413 (1976).
[23] A. Srinivasan, K. Jagannathan, M. S. Hedge, and C. N. R. Rao, Indian J. Chem. A **18**, 463 (1979).